

Rapid measurement and correction of spatiotemporal B_0 field changes using FID navigators and a multi-channel reference image

Tess E. Wallace^{1,2}  | Onur Afacan^{1,2}  | Tobias Kober^{3,4,5} | Simon K. Warfield^{1,2}

¹Computational Radiology Laboratory, Department of Radiology, Boston Children's Hospital, Boston, Massachusetts

²Harvard Medical School, Boston, Massachusetts

³Advanced Clinical Imaging Technology, Siemens Healthcare AG, Lausanne, Switzerland

⁴Department of Radiology, Lausanne University Hospital and University of Lausanne, Lausanne, Switzerland

⁵LTS5, École Polytechnique Fédérale de Lausanne, Lausanne, Switzerland

Correspondence

Tess E. Wallace, Computational Radiology Laboratory, Boston Children's Hospital, 360 Longwood Avenue, Boston, MA 02215.
Email: tess.wallace@childrens.harvard.edu

Funding information

National Institutes of Health, Grant/Award Numbers: R01 EB019483, R01 NS079788, R01 DK100404, R44 MH086984, IDRC U54 HD090255; Early Career Award from the Thrasher Research Foundation.

Purpose: To measure spatiotemporal B_0 field changes in real time using FID navigators (FIDnavs) and to demonstrate the efficacy of retrospectively correcting high-resolution T_2^* -weighted images using a novel FIDnav framework.

Methods: A forward model of the complex FIDnav signals was generated by simulating the effect of changes in the underlying B_0 inhomogeneity coefficients, with spatial encoding provided by a multi-channel reference image. Experiments were performed at 3T to assess the accuracy of B_0 field estimates from FIDnavs acquired from a 64-channel head coil under different shim settings and in 5 volunteers performing deep-breathing and nose-touching tasks designed to modulate the B_0 field. Second-order, in-plane spherical harmonic (SH) inhomogeneity coefficients estimated from FIDnavs were incorporated into an iterative reconstruction to retrospectively correct 2D gradient-echo images acquired in both axial and sagittal planes.

Results: Spatiotemporal B_0 field changes measured from rapidly acquired FIDnavs were in good agreement with the results of second-order SH fitting to the measured field maps. FIDnav field estimates accounted for a significant proportion of the ΔB_0 variance induced by deep breathing ($64 \pm 21\%$) and nose touching ($67 \pm 34\%$) across all volunteers. Ghosting, blurring, and intensity modulation artifacts in T_2^* -weighted images, induced by spatiotemporal field changes, were visibly reduced following retrospective correction with FIDnav inhomogeneity coefficients.

Conclusions: Spatially resolved B_0 inhomogeneity changes up to second order can be characterized in real time using the proposed approach. Retrospective FIDnav correction substantially improves T_2^* -weighted image quality in the presence of strong B_0 field modulations, with potential for real-time shimming.

KEYWORDS

B_0 inhomogeneity, FID navigators, retrospective artifact correction, spatiotemporal field changes

1 | INTRODUCTION

Accurate image encoding in MRI relies on exact knowledge of the underlying magnetic field gradients, which are designed to vary linearly across the imaging volume. In the presence of B_0 field inhomogeneities, higher-order gradients cause a variety of image artifacts including ghosting, blurring and signal loss in T_2^* -weighted imaging,¹ and unwanted macroscopic phase changes in SWI.² Field distortions arise from the underlying magnetic susceptibility distribution in the head, particularly in regions near air–tissue interfaces such as the frontal sinus, nasal cavities, and ear canals, as well as imperfections in the main magnet and gradient fields. MRI scanners automatically perform a shimming process before scanning by measuring a low-resolution field map and superimposing an optimal combination of low-spatial-order spherical harmonic (SH) fields on the static magnetic field. Although this helps to improve static B_0 homogeneity for the subject-specific susceptibility distribution, it does not account for dynamic B_0 fluctuations that occur over the course of the scan because of system instabilities, subject motion, and other physiological processes. Respiration induces time-varying magnetic susceptibility distributions in the brain because of movement of the chest wall, changing lung volume, and fluctuations in local oxygen concentrations.^{3,4} Motion, both inside and outside the imaging volume, also alters the susceptibility distribution, giving rise to spatially varying B_0 changes.^{5,6} As these susceptibility effects scale with the applied magnetic field, they become increasingly important at higher field strengths, where artifacts are more pronounced.⁷

To compensate for these time-varying effects, B_0 field changes must be monitored and either the shim currents must be updated during the scan (dynamic or real-time shimming) or the effects of ΔB_0 must be considered in the reconstruction. Commercial MRI scanners often apply dynamic correction to account for global frequency drift in sensitive applications such as EPI and spectroscopy. External field probes positioned around the subject may be used to dynamically sample spatiotemporal field changes during imaging for real-time field control⁸ or retrospective artifact correction.^{9,10} This method requires that low-spatial-order field maps be fitted to these point measurements using either SH expansion^{8,11} or training data¹² to extrapolate field changes in the head region, which may limit accuracy. Methods that estimate field changes from the MR data itself are advantageous as they measure ΔB_0 directly within the brain, without the need for any additional hardware. FID navigators (FIDnavs) have traditionally been used to compensate for global frequency fluctuations in fMRI^{13,14} and can be rapidly acquired with minor sequence modifications. Zeroth-order correction can also yield some improvement in structural scans, for example correcting for respiration in axial slices where the dominant effect

manifests as a global frequency shift,¹ but is inadequate in other scenarios because of the spatial heterogeneity of the induced field changes. To provide spatially resolved field estimates, multiple 1D navigators of the projections may be acquired along orthogonal axes.^{15,16} First-order B_0 changes may then be calculated in each readout direction by measuring the shifts in the center of k-space or the phase evolution between 2 gradient echoes separated by time $\Delta\tau$. Three-dimensional dual-echo navigators may be used to further improve spatially resolved field estimates,^{17,18} however, these take a long time to acquire meaning there is a trade-off between the spatial resolution of measurements and the increase in scan time. Segmented navigators can be used to reduce the additional scan time needed, but at the cost of temporal resolution. Therefore, most current methods are limited to infrequent, “global” field measurements over the imaging volume, which is insufficient, particularly near regions with large magnetic susceptibility changes. Slice-by-slice ΔB_0 correction would be more beneficial to correct for highly localized field changes within the brain.

Several approaches have used additional information provided by multi-channel receive coil arrays or training data to enable spatially resolved field maps to be measured from rapidly acquired navigator echoes with or without gradient encoding. For example, the phase changes from FID and frequency-encoded navigators can be weighted by the coil sensitivity profile at each location to provide an approximation of the spatial field distribution.⁵ Other approaches make use of the fact that the number of adjustable shim correction fields is already limited and use additional encoding information to transform a small amount of k-space data directly into field inhomogeneity coefficients.^{19,20} Van Gelderen et al¹⁹ modeled the effect of second-order shim currents on phase changes in a phantom, followed by subject-specific training to calibrate navigator phase changes as a function of chest motion information acquired during the scan, however, this method only corrects for periodic phase variations linearly related to measured chest position. Another approach is to directly model the FIDnav as a weighted integral of the spin density distribution and field inhomogeneities, modulated by the coil sensitivity at each point. Splitthoff and Zaitsev²⁰ proposed estimating low-order shim coefficients from the temporal evolution (slope) of FIDnavs by expressing the FIDnav as a projection of a multi-channel reference image. Although this study demonstrated proof-of-principle of this method on phantom data, implicit assumptions about tissue relaxation and chemical heterogeneity, which are known to influence the temporal evolution of the complex FIDnav signal, are problematic for in vivo imaging.

In this study, we propose an alternative method to rapidly measure spatiotemporal field changes from FIDnavs by simulating the effect of low-spatial-order field changes using encoding provided by a complex multi-channel

reference image. Rather than estimating ΔB_0 from the temporal evolution of the FIDnav signal, we consider the effect of underlying shim changes on FIDnav measurements sampled at the TE of the reference image. Solving the inverse problem posed by the FIDnavs yields the change in ΔB_0 inhomogeneity coefficients over time. The main contributions of this work are as follows

1. Creation of a forward model that describes the effect of ΔB_0 on the measured FIDnav signal in each slice using a low-resolution multi-channel reference image and simulated shim coefficient changes.
2. Rapid estimation of up to second-order, in-plane inhomogeneity coefficients from FIDnavs acquired under different scanner shim settings and in volunteers performing tasks designed to induce strong B_0 fluctuations.
3. Retrospective correction of T_2^* -weighted images using an iterative reconstruction algorithm to compensate for spatiotemporal B_0 changes measured from FIDnavs.

2 | METHODS

2.1 | FID navigator field measurement framework

FIDnavs measure the signal received by each element in a coil array without any gradient encoding. In the presence of spatially varying coil sensitivities and static field inhomogeneities, the FIDnav signal $y_{j,0}(\tau)$ from channel j , sampled at time τ at a reference point (denoted acquisition index 0), may be represented as

$$y_{j,0}(\tau) = \int_v c_j(\mathbf{r}) \cdot \rho(\mathbf{r}, \tau) \cdot \exp(i\varphi_j(\mathbf{r})) \cdot \exp(i\gamma\tau\Delta B_0(\mathbf{r})) d\mathbf{r} \\ = \int_v s_{j,0}(\mathbf{r}, \tau) d\mathbf{r} \quad (1)$$

where $c_j(\mathbf{r})$ represents the spatial sensitivity profile of the j th coil; $\rho(\mathbf{r}, \tau)$ is the effective spin density at TE τ (accounting for relaxation, excitation profile etc.); $\varphi_j(\mathbf{r})$ is the phase contribution arising from the transmit and receive coils; γ is the gyromagnetic ratio (in $\text{rads}^{-1}\text{T}^{-1}$); $\Delta B_0(\mathbf{r})$ describes the spatial magnetic field inhomogeneity; and \mathbf{r} is the spatial coordinate within the excited volume. For 2D slice-selective imaging, $\mathbf{r}=(x,y)$ and the integral is performed over the excited slice, although the method is easily extendable to 3D. This may also be expressed as the integral of a reference image $s_{j,0}(\mathbf{r}, \tau)$ measured by the j th coil with TE τ . Using this information, an FIDnav at acquisition n may be written

$$y_{j,n}(\tau) = \int_v c_j(\mathbf{r}) \cdot \rho(\mathbf{r}, \tau) \cdot \exp(i\varphi_j(\mathbf{r})) \cdot \exp(i\gamma\tau[\Delta B_0(\mathbf{r}) + \delta B_{0,n}(\mathbf{r})]) d\mathbf{r} \\ = \int_v s_{j,0}(\mathbf{r}, \tau) \cdot \exp(i\gamma\tau\delta B_{0,n}(\mathbf{r})) d\mathbf{r} \quad (2)$$

where $\delta B_{0,n}(\mathbf{r})$ is the change in field inhomogeneity at acquisition n , relative to the reference acquisition, and is considered to be constant during the readout time.

Spatiotemporal variations in the magnetic field δB_0 may be represented by a series of low-order SH fields as follows:

$$\delta B_0(\mathbf{r}, n) = \boldsymbol{\beta}(\mathbf{r}) \mathbf{b}(n), \quad (3)$$

where $\boldsymbol{\beta}(\mathbf{r})$ is an $N_p \times N_b$ matrix representing the N_b basis functions for an image with N_p pixels, and $\mathbf{b}(n)$ is an $N_b \times 1$ vector representing the coefficients at acquisition n . By stacking information from N_c receiver coils, and approximating integration as a complex summation of pixel intensities, Equation 2 may be written in matrix form as

$$\begin{bmatrix} y_{1,n} \\ y_{2,n} \\ \vdots \\ y_{N_c,n} \end{bmatrix} = \begin{bmatrix} S_{1,0} \\ S_{2,0} \\ \vdots \\ S_{N_c,0} \end{bmatrix} \exp(i\gamma\tau\boldsymbol{\beta}\mathbf{b}_n), \quad (4)$$

where $y_{j,n}$ is the measured FIDnav from coil j at acquisition n and $S_{j,0}$ is a $1 \times N_p$ vector of the reference complex coil image pixel intensities.

A forward model can be generated by simulating the effect of changes in the underlying inhomogeneity coefficients on the complex FIDnavs (Equation 4). If δB_0 is sufficiently small (i.e., $\exp(x) \approx 1+x$), changes in the FIDnav signal may be assumed to be linear with respect to the field inhomogeneity coefficients. A calibration matrix A may then be determined by simulating step changes in the underlying SH inhomogeneity coefficients b_k , so that each element $A_{j,k} = S_{j,0} \exp(i\gamma\tau\boldsymbol{\beta}_k b_k)$. A schematic of this framework is shown in Figure 1. Considering the real and imaginary parts of the complex FIDnav signal vector \mathbf{Y} and calibration matrix A , which is of size $N_c \times (N_b + 1)$, results in the following overdetermined system of equations

$$\begin{bmatrix} \Re(\mathbf{Y}) \\ \Im(\mathbf{Y}) \end{bmatrix} = \begin{bmatrix} \Re(A) \\ \Im(A) \end{bmatrix} [\mathbf{1} \mathbf{b}^T]. \quad (5)$$

The unknown coefficients \mathbf{b} describing the inhomogeneity coefficients can then be computed using least-squares fitting to solve the inverse problem posed by the measured FIDnavs.

2.2 | Multi-channel reference image

FIDnavs represent the integral of each voxel's contribution (determined by spin density, field inhomogeneities, and TE), weighted by the coil sensitivity at each spatial location. Therefore, discrete summation of the complex pixel values

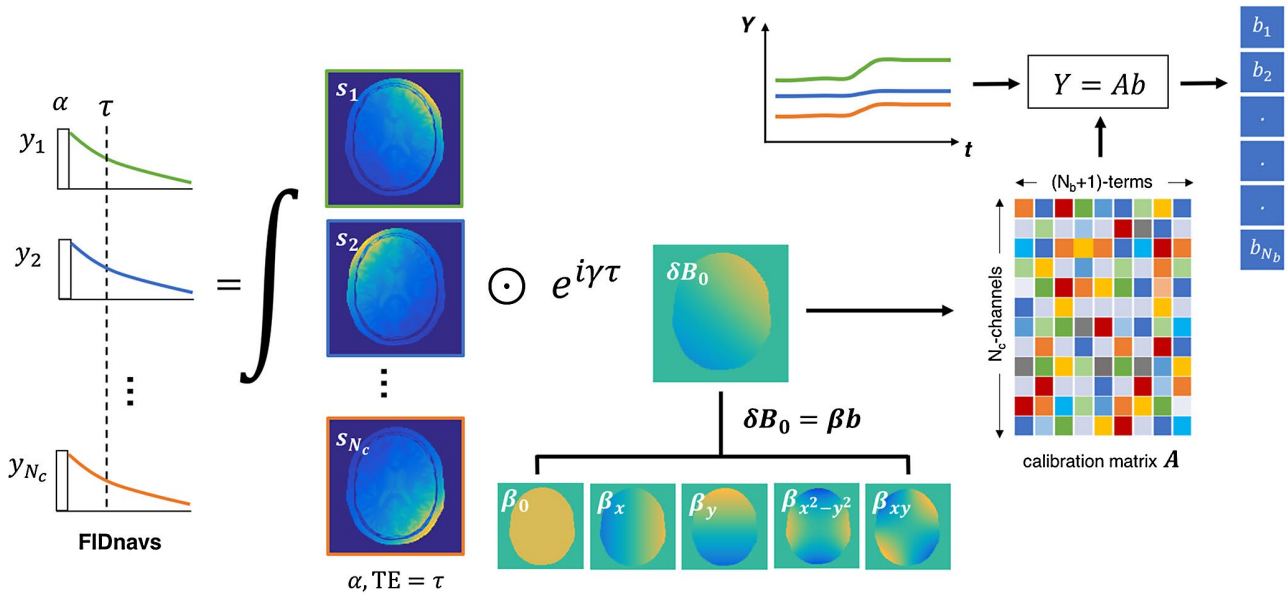


FIGURE 1 Schematic showing construction of a forward model of FIDnav data points from a multi-channel reference image and simulated step changes in B_0 field inhomogeneity coefficients. Dynamic field changes may be estimated using this calibrated model by solving the inverse problem posed by the rapidly acquired FIDnavs in each slice

in images measured by each coil may be used to simulate the FIDnav signal, as described above. However, gradient delays, eddy currents, and other system imperfections cause small deviations in gradient encoding, giving rise to small phase offsets and distortions in images acquired with Cartesian sampling. To mitigate these effects, a pair of reference images were acquired with high readout bandwidth (to minimize distortion) and opposite gradient polarities. Low-resolution images were reconstructed by applying an elliptical filter to the raw k-space data to minimize Gibb's ringing, and the phase error was estimated via a weighted sum over channels of the Hermitian inner product

$$\hat{\theta}(\mathbf{r}) = \text{angle} \left(\frac{1}{N_c} \sum_{j=1}^{N_c} \frac{s_j^+(\mathbf{r}) \cdot s_j^-(\mathbf{r})^*}{|s_j^+(\mathbf{r})|} \right), \quad (6)$$

where s_j^+ and s_j^- refer to the images acquired from the j th coil with opposite gradient polarities and s^* denotes the complex conjugate. The reference image was estimated by combining the phase-corrected data as follows

$$s_j(\mathbf{r}) = s_j^+(\mathbf{r}) \exp(-i\hat{\theta}(\mathbf{r})/2) + s_j^-(\mathbf{r}) \exp(i\hat{\theta}(\mathbf{r})/2). \quad (7)$$

2.3 | MR data acquisition

All phantom and volunteer experiments were performed on a whole-body 3T MRI scanner (MAGNETOM Skyra, Siemens Healthcare, Erlangen, Germany) equipped with quadrature transmit and a 64-channel phased array head coil. A product FLASH sequence was modified to acquire an FIDnav

following each slice-selective radiofrequency excitation and before the imaging readout. Five volunteers (2 female; aged 28–37 y) were scanned after providing written informed consent in accordance with the Institutional Review Board-approved protocol.

2.4 | Experiment 1: accuracy of FIDnav B_0 field measurements with changing shim settings

A doped water bottle phantom was scanned with changing first- and second-order shim settings on the scanner. A single axial slice was acquired through the isocenter, and shim currents corresponding to the SH functions X , Y , X^2-Y^2 and $2XY$ were manually altered in between each scan. The experiment was divided into 4 sequential blocks: first-order shim settings were adjusted in the range $\pm 4 \mu\text{T/m}$ in increments of $1 \mu\text{T/m}$; second-order shim settings were adjusted in the range $\pm 50 \mu\text{T/m}^2$ in increments of $12.5 \mu\text{T/m}^2$. This range of values was chosen to give a comparable maximum frequency change within the phantom²⁰ and represents the scale of shim changes previously observed in volunteer experiments.¹⁵ The experiment was then repeated on a volunteer, who was instructed to lie still in the magnet for the duration of imaging.

Before each measurement block, a pair of 2D FLASH reference images with opposite gradient polarities were acquired (total acquisition time ~ 13 s). A dual-echo FID-navigated sequence was acquired for each shim setting. Scan parameters for the reference and FID-navigated

scans are given in Table 1. Two averages of the FID-navigated sequence were acquired, resulting in 128 FIDnavs for each acquisition (1 for each phase-encoding step). Measurements from the first 4 s were discarded to allow the FIDnav signal to reach a steady state. The FIDnav ADC readout sampled a total of 320 points in 4 ms. To match the contrast properties of the reference image, 10 complex FIDnav readout samples centered on TE = 4 ms were averaged, generating a single measurement for each coil and phase-encoding step. The resulting FIDnav time-course was median-filtered (window size = 3) before dynamic field estimation. Phase-corrected reference images from each channel were reconstructed as described above. Zeroth-, first-, and second-order changes in the in-plane shim coefficients (normalized to induce a 0.1 μ T change at 0.1 m from the isocenter) were simulated to calibrate the model matrix A . The inverse of Equation 5 was solved to yield field inhomogeneity coefficients describing variations up to second order ($N_b = 5$). We also tested directly solving for the field inhomogeneity coefficients (Equation 4) using a non-linear optimization algorithm²¹ and compared this with the linear approximation. This yielded highly similar results (see Supporting Information Figure S1), and therefore the linear approximation was used in the remainder of the experiments.

Conventional field mapping was also performed for comparison by calculating the pixel-wise phase difference between the multi-channel dual-echo data as follows

$$\Delta B_0(\mathbf{r}) = \frac{1}{\gamma \Delta TE} \text{angle} \left(\frac{1}{N_c} \sum_{j=1}^{N_c} \frac{s_{j,1}(\mathbf{r}) \cdot s_{j,2}(\mathbf{r})^*}{|s_{j,2}(\mathbf{r})|} \right), \quad (8)$$

where ΔTE is the difference in TEs. To reduce noise, field maps were filtered using a 3×3 median filter and SH functions up to second-order were fit within the foreground region, determined by intensity thresholding. FIDnav field coefficients were compared to those obtained by direct SH fitting. To enable direct comparison of the field maps obtained by the proposed FIDnav method $B_0^{est,FID}(\mathbf{r}, n)$ and the results of SH fitting $B_0^{est,SH}(\mathbf{r}, n)$ to pixel-wise field maps $B_0^{ref}(\mathbf{r}, n)$ (considered the “gold-standard” method for shimming), the relative mean sum-of-squares error (rMSSE) was calculated within the masked region as follows¹²

$$rMSSE = \frac{\langle (\Delta(\mathbf{r}, n) - \langle \Delta(\mathbf{r}, n) \rangle_n)^2 \rangle_{ROI}}{\langle (B_0^{ref}(\mathbf{r}, n) - \langle B_0^{ref}(\mathbf{r}, n) \rangle_n)^2 \rangle_{ROI}}, \quad (9)$$

where $\Delta(\mathbf{r}, n) = B_0^{est}(\mathbf{r}, n) - B_0^{ref}(\mathbf{r}, n)$ and $\langle \cdot \rangle_n$ and $\langle \cdot \rangle_{ROI}$ denote the temporal average and both temporal and spatial average within the ROI, respectively. The temporal mean is removed in the calculation of rMSSE as constant B_0 offsets do not result in any image degradation.¹²

TABLE 1 Data acquisition parameters for 2D FLASH imaging experiments

Scan	FIDnav τ (ms)	TR (ms)	TE ₁ /TE _N (ms)	α (°)	Matrix size	Resolution (mm)	Slice Δz [spacing] (mm)	Slices (N)	rBW (Hz/px)
Single-slice low-resolution dynamic field mapping									
Reference	–	100	4.0	20	64×64	4×4	4	1	1240
FID-navigated	4.0	100	6.9/8.4	20	64×64	4×4	4	1	1240
Single-slice high-resolution structural imaging									
Reference	–	400	4.0	30	64×64	4×4	3	1	1240
FID-navigated	4.0	400	10.5/46.0 ($\Delta TE = 7.1$)	30	512×512	0.5×0.5	3	1	256
Multi-slice high-resolution structural imaging									
Reference	–	600	4.0	30	64×64	4×4	3 [0.6]	10	1240
FID-navigated	4.0	600	10.5/46.0 ($\Delta TE = 7.1$)	30	512×512	0.5×0.5	3 [0.6]	10	256

Abbreviations: α , flip angle; rBW, readout bandwidth; τ , FIDnav sampling time; Δz slice thickness. All 2D FLASH scans acquired with field of view 256×256 mm and no acceleration.

2.5 | Experiment 2: evaluation of FIDnav ΔB_0 field measurements during deep-breathing and nose-touching tasks

In this experiment, volunteers were asked to perform tasks designed to modulate the B_0 field while FIDnavs and dynamic field maps were acquired simultaneously. Subjects were asked to (1) lie still and breathe normally; (2) take deep breaths, holding inhale and exhale respiratory positions (deep-breathing); and (3) move their arm to touch their nose in discrete steps (nose-touching). FID-navigated 2D FLASH scans were acquired in both axial and sagittal orientations to examine the field changes in different directions. Scan parameters were the same as those used in the previous experiment (Table 1). Head motion was monitored over the course of the scan using an electromagnetic tracking system (Robin Medical, Baltimore, MD) comprising 4 sensors placed on the subject's forehead, which measure position and orientation in real time.²²

FIDnav inhomogeneity coefficients were computed as described above. To provide ground-truth measurements of spatiotemporal field changes, a series of 15 low-resolution dual-echo images were acquired for each paradigm. Field changes were estimated relative to the baseline field map, and ground-truth SH coefficients were calculated by fitting to the measured pixel-wise data in the foreground region, as described above. Field maps computed from the FIDnav and fitted SH coefficients were compared to the measured pixel-wise field maps by evaluating the rMSSE. One-sample t-tests were performed to determine if the reduction in rMSSE was significantly different from 0.

2.6 | Experiment 3: retrospective correction of high-resolution gradient-echo scans

High-resolution 2D FLASH scans were also acquired for each subject to examine any improvements in image quality that could be achieved by incorporating FIDnav field estimates into the reconstruction. Three scans were acquired for each paradigm: volunteers were instructed to (1) lie still and breathe normally; (2) breathe deeply for the duration of the scan; and (3) repeatedly raise their arm to touch their nose. Reference and high-resolution structural images were acquired for a single slice in both axial and sagittal orientations. High-resolution images were acquired with multiple echoes to enable comparison of artifacts and reconstruction quality with increasing T_2^* -weighting. Multi-slice axial scans were also acquired for 2 subjects to confirm that acquiring multiple interleaved slices did not affect the ability of FIDnavs to estimate in-plane shim parameters. Scan parameters are displayed in Table 1. The total time taken to acquire the reference data was 51 s and 77 s for the single-slice and multi-slice acquisitions, respectively.

Retrospective correction of second-order phase errors was performed using an iterative reconstruction approach.⁵ FIDnav field estimates were incorporated into the image-encoding equation, which can be written in matrix form as follows

$$\mathbf{k}_j = \mathbf{E} \mathbf{S}_j = \sum_i \mathbf{M}_i \mathbf{F}(\mathbf{P}_i \cdot \mathbf{S}_j), \quad (10)$$

where \mathbf{k}_j is a $[N_k \times 1]$ vector of the sampled k-space data from the j th coil, \mathbf{E} is the encoding matrix, extended to contain both Fourier-encoding terms and phase errors for each k-space shot $E_{k,u} = \exp(-i[k_k \cdot x_u + \delta\omega_0(r_u)])$, and \mathbf{S}_j is an $[N_p \times 1]$ vector of the image pixel intensities. Because \mathbf{E} is of size $[N_k, N_p]$, it becomes prohibitively large, even for moderate imaging resolutions. Therefore, an iterative approach was used that calculates the relevant parts of \mathbf{E} and its conjugate \mathbf{E}^H for each segment of k-space denoted by the mask \mathbf{M}_i ; \mathbf{F} is the Fourier transform operator and $\mathbf{P}_i = \exp(i\gamma\tau\mathbf{B}\mathbf{b}_i)$ is a $[N_p \times 1]$ vector of phase errors corresponding to the i th k-space segment. The maximum number of iterations was set to 3 as an ad hoc measure to limit reconstruction times; k-space data from each channel was compressed into 16 virtual coils to further accelerate reconstruction.²³ Complex image data from each virtual coil was combined using the adaptive-combine algorithm.²⁴

The first image in each set, acquired without any intentional B_0 field variations, was used as a reference to assess the performance of the proposed method for compensating for spatiotemporal field inhomogeneities. Each image was registered to the corresponding reference image, and normalized root-mean-square error (NRMSE) within a masked region determined by intensity thresholding was calculated for images reconstructed with and without retrospective correction.

3 | RESULTS

3.1 | Experiment 1: accuracy of FIDnav B_0 field measurements with changing shim settings

Figure 2 shows the mean and SD of the estimated inhomogeneity coefficients from FIDnav measurements in a phantom and volunteer scan where the scanner shim currents were systematically modified. Coefficients estimated by directly fitting second-order SH functions to measured pixel-wise field maps are also shown for comparison. The shim coefficients measured from both FIDnavs and direct fitting demonstrate a high correlation with the applied values, although some cross-term fields are evident. In the phantom scan, comparison between FIDnav field coefficient estimates and direct SH fitting yielded mean absolute errors of $0.061 \pm 0.057 \mu\text{T/m}$ (for maximum changes of $4 \mu\text{T/m}$) and $0.601 \pm 0.926 \mu\text{T/m}^2$ (for maximum changes of $50 \mu\text{T/m}^2$). In the volunteer

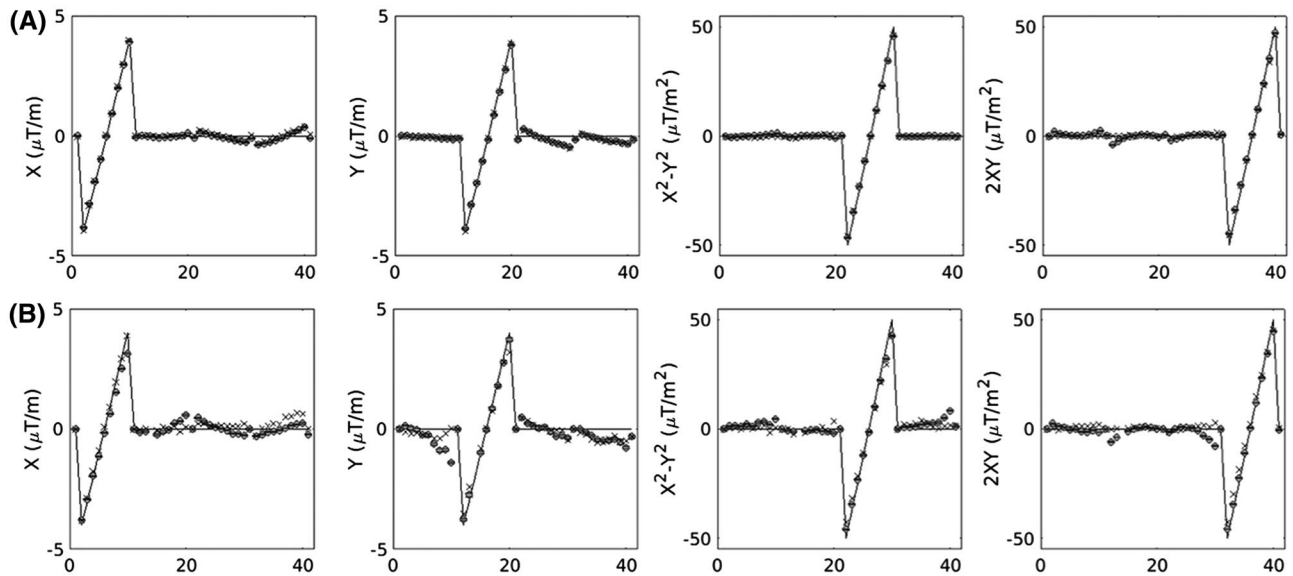


FIGURE 2 First-order (X and Y) and second-order (X^2-Y^2 and $2XY$) shim changes measured in phantom (A) and volunteer (B) experiments. Solid line denotes the applied shim currents; filled circles with error bars show the mean and standard deviation of FIDnav measurements in each scan; gray crosses denote results of direct SH fitting to pixel-wise field maps. FIDnav shim estimates demonstrate a high correlation with the applied values in both phantom and in vivo scans

scan, mean absolute errors were $0.231 \pm 0.345 \mu\text{T/m}$ and $1.85 \pm 2.55 \mu\text{T/m}^2$. Applying FIDnav field estimates corresponded to a mean reduction in rMSSE of 98.4% and 76.6% in the phantom and volunteer scans, respectively (compared to 99.4% and 97.0% for direct SH fitting).

3.2 | Experiment 2: evaluation of FIDnav ΔB_0 field measurements in vivo

Both deep-breathing and nose-touching tasks induced substantial spatiotemporal variations in the B_0 field. Head motion was monitored during each scan, and root-sum-of-squares translations and rotations across all volunteers were $0.25 \pm 0.20 \text{ mm}$ and $0.22 \pm 0.36^\circ$. For all scans, over 99% of translational motions and 96% of rotational motions remained within 1 mm and 1° , respectively. The estimated changes in inhomogeneity coefficients in the sagittal plane during deep breathing are shown in Figure 3A. Pixel-wise ΔB_0 maps computed relative to the baseline scan for inhale and exhale respiratory positions are shown in Figure 3B, alongside the results of second-order SH fitting and maps generated from the estimated FIDnav inhomogeneity coefficients. Maximum changes of up to 24.5 Hz were observed in the brainstem during deep breathing. A comparison of zeroth-, first-, and second-order FIDnav and SH inhomogeneity coefficients across all volunteers performing the deep breathing task in the sagittal plane is shown in Supporting Information Figure S2. FIDnav inhomogeneity coefficients measured in the axial plane during nose touching, and the corresponding field maps are shown in Figure 4. Strong inhomogeneities of up

to 19.4 Hz were observed in the frontal brain region. Maps generated from the measured FIDnav coefficients are in excellent agreement with those computed by directly fitting SH functions to the measured field maps. Mean absolute errors between FIDnav and SH inhomogeneity coefficients for deep-breathing and nose-touching tasks in axial and sagittal planes are summarized in Supporting Information Table S1.

The rMSSE (relative to the measured pixel-wise maps) for “gold-standard” SH fitting and the proposed FIDnav method are shown in Figure 5. This gives an estimate of the percentage of the ΔB_0 variance explained by each approach. Values below 100% demonstrate a reduction in spatial ΔB_0 inhomogeneity, compared to no correction. For the deep-breathing experiment, mean reductions in rMSSE of $68 \pm 26\%$ (axial) and $61 \pm 15\%$ (sagittal) were achieved using our proposed FIDnav approach. For nose touching, reductions in rMSSE were $80 \pm 17\%$ (axial) and $55 \pm 44\%$ (sagittal). FIDnav correction resulted in a significant ($P < 0.05$) improvement in residual inhomogeneity for deep breathing in both axial and sagittal orientations, and for nose touching in axial orientation.

3.3 | Experiment 3: retrospective correction of high-resolution gradient-echo scans

Retrospective correction results for high-resolution structural imaging in the sagittal plane during deep breathing are shown in Figure 6A for different TEs. The 5 SH coefficients measured by FIDnavs during continuous deep breathing are shown in Figure 6B. Deep breathing induces substantial

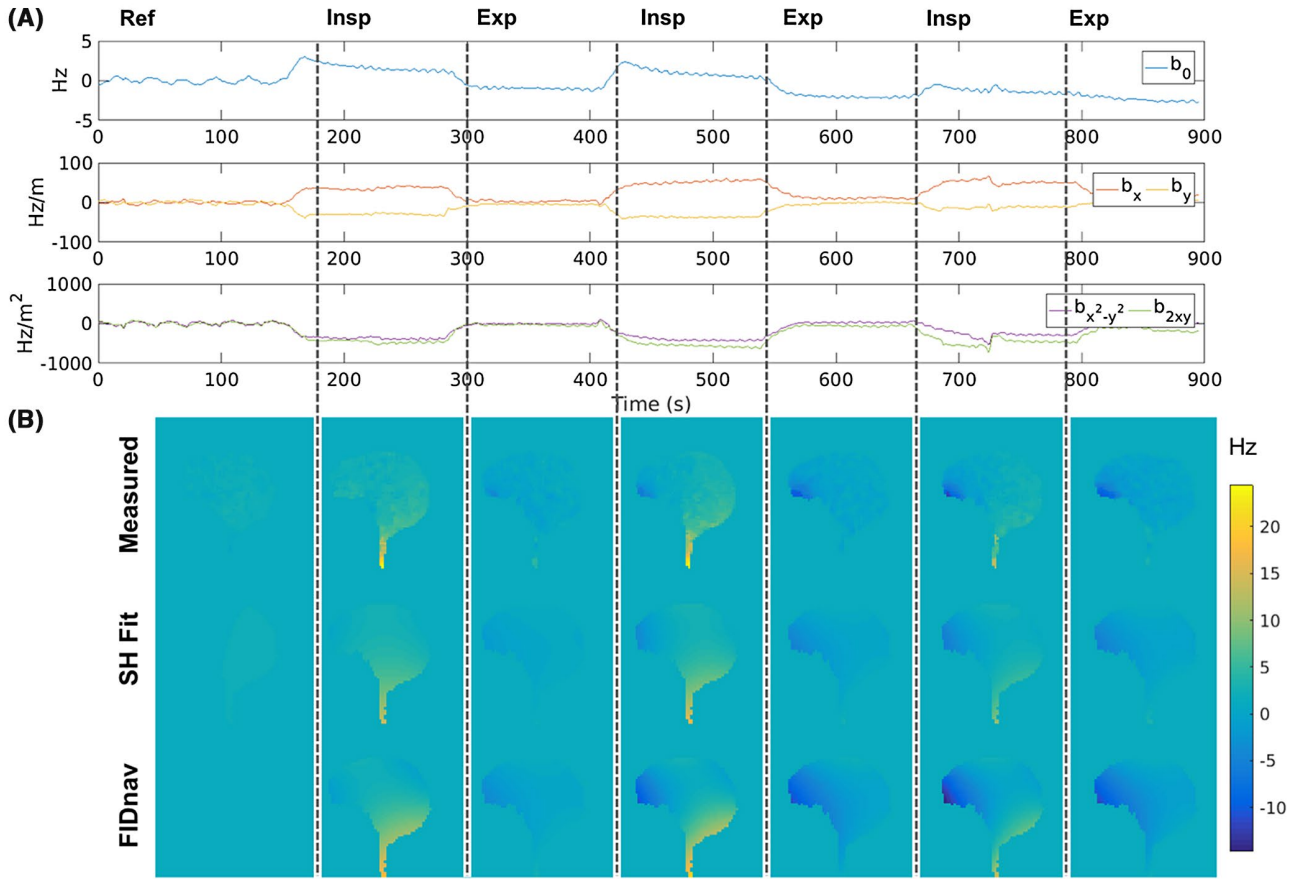


FIGURE 3 Dynamic zeroth-, first-, and second-order ΔB_0 field inhomogeneity coefficients measured from FIDnavs in a 2D slice in the sagittal plane during inspiration and expiration (A). Comparison of ground-truth ΔB_0 field maps measured during inhale and exhale breath-holds, results of direct second-order SH fitting in the masked region, and field maps estimated from FIDnav inhomogeneity coefficients (B)

ghosting artifacts, particularly for more inferior brain regions that are closer to the lungs. Ghosting becomes more severe with longer TEs; for strongly T_2^* -weighted images, anatomic information in the cerebellum and brainstem is destroyed (Figure 6C). Image quality is visibly improved following retrospective correction with FIDnav field estimates across all TEs. Similarly, Figure 7A demonstrates a clear improvement in the quality of high-resolution axial images following dynamic FIDnav field correction for the nose-touching task. Field disturbances, particularly in frontal brain regions, result in substantial ghosting and blurring artifacts, which are visibly reduced following retrospective correction. Boxplots of NRMSE (computed for the longest TE) before and after correction, relative to the image acquired with no intentional ΔB_0 modulations, are shown for the deep-breathing and nose-touching tasks in Figure 8. NRMSE decreased for all volunteers in both axial and sagittal orientations. The percentage reduction in NRMSE for the deep-breathing task was $19.0 \pm 4.7\%$ for axial scans and $13.3 \pm 10.4\%$ for sagittal scans. For nose touching, reduction in NRMSE was $19.2 \pm 16.4\%$ (axial plane) and $10.1 \pm 11.7\%$ (sagittal plane).

Examples of retrospective correction for slice-wise field inhomogeneities in axial multi-slice images are shown in

Figure 9. Deep-breathing and nose-touching tasks resulted in substantial intensity modulations and ghosting, with stronger artifacts evident in more inferior brain regions, corresponding to larger inhomogeneity coefficients measured in this slice (Supporting Information Figure S3). Artifacts were visibly reduced following retrospective correction, demonstrating the ability of the proposed technique to compensate for field inhomogeneities on a slice-by-slice basis.

Reconstruction time was ~ 40 s per channel and slice, using the proposed iterative reconstruction algorithm implemented in MATLAB R2016b (The MathWorks, Natick, MA). Coil compression reduced overall reconstruction times by a factor of 4, while maintaining highly similar image quality (see Supporting Information Figure S4).

4 | DISCUSSION

4.1 | Accuracy of field monitoring

In this work, we propose a novel framework for measuring spatially resolved dynamic field changes from rapidly acquired multi-channel FIDnavs with no gradient encoding. To assess the accuracy of the proposed method, we

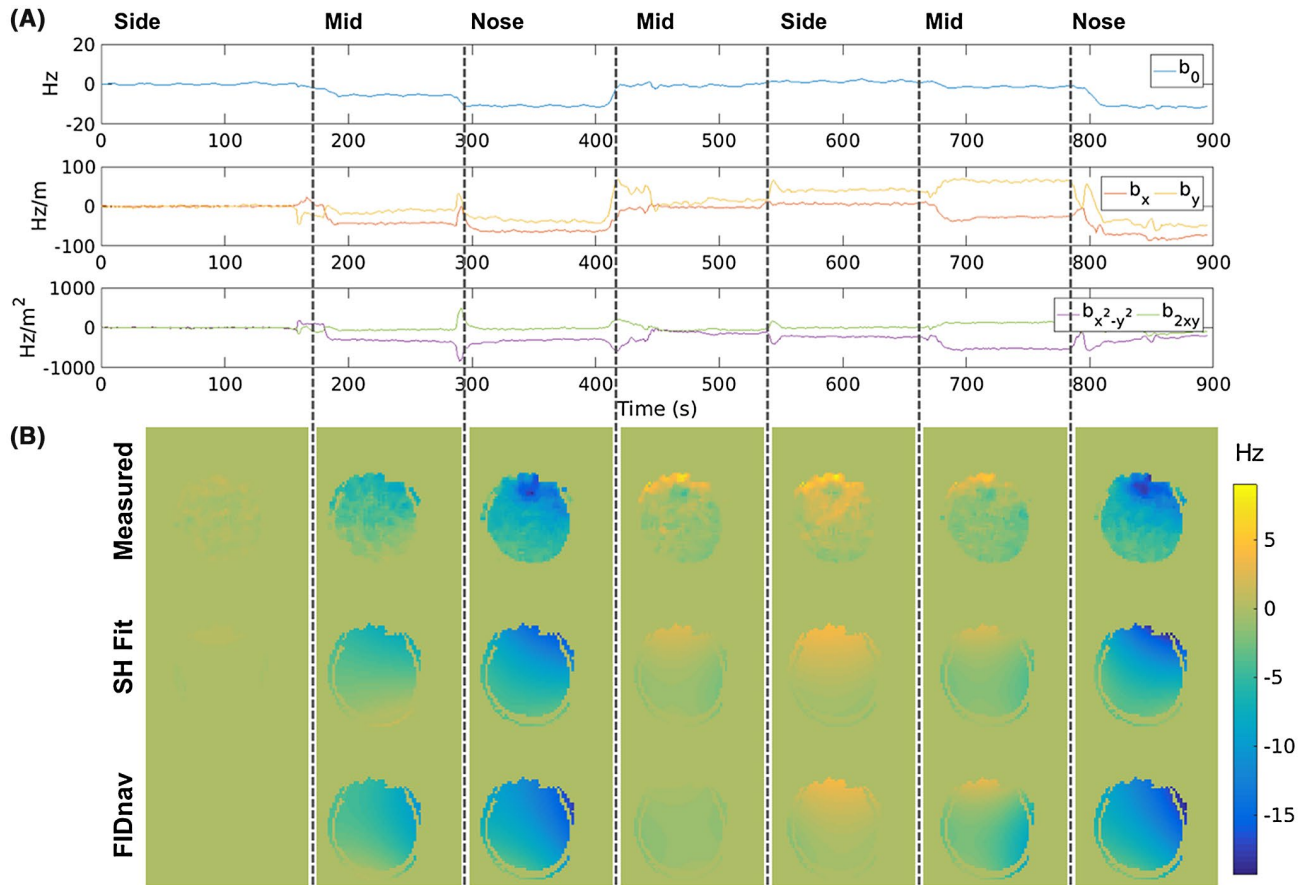


FIGURE 4 Dynamic ΔB_0 field inhomogeneity coefficients measured in a 2D axial slice during nose touching (A). Comparison of ground-truth ΔB_0 field maps in the arm-by-side, mid-way and nose-touching positions, second-order SH fit in the masked region and field maps estimated from FIDnav inhomogeneity coefficients (B)

compared field maps generated from FIDnav inhomogeneity coefficients to the results of directly fitting second-order SH functions to measured pixel-wise field maps in a series of phantom and volunteer experiments. This is the gold standard method used for static shimming on most scanners; however, direct fitting has limited applicability for real-time shimming because of the time taken to acquire a spatially resolved dual-echo image. FIDnav B_0 measurements exhibited high correlation with applied shim current changes up to second order in both phantom and volunteer experiments. Changing the second-order shim terms $X^2 - Y^2$ and $2XY$ produced some additional linear fields in X and Y , which may be because of long-time constant eddy currents induced by second-order shim switching.²⁵ Estimated shim coefficients were in excellent agreement with the gold standard image-based SH fitting results but FIDnav measurements can be acquired in a fraction of the time and without disturbing the sequence.

In volunteers, deep breathing and nose touching induced strong susceptibility variations in both axial and sagittal planes, with maximum observed field changes consistent with previous studies.^{4,5} Second-order FIDnav field measurements accounted for a significant proportion of the spatiotemporal

field variations induced by both tasks, which were designed to mimic “worst-case scenario” field changes. Applying second-order FIDnav field correction for no motion and normal breathing (where field changes at 3T are minimal) did not result in any significant differences. Residual differences may also be explained in part by noise in the pixel-wise field maps.

In-plane SH coefficients up to second order were measured in this study, as this represents the range of possible correction fields currently available on most scanners. Solving for third-order (or higher) changes is possible using high-channel-count coil arrays and enables modeling of more complex field distributions; however, increasing the number of coefficients also makes the system more sensitive to noise. We did not find significant differences between fitting for first-, second-, or third-order inhomogeneity coefficients with FIDnavs for the field changes tested in this work (Supporting Information Figure S5). This suggests that first-order FIDnav field measurements could be used to update the gradient offsets, providing a practical solution for real-time field correction at 3T without the requirement for dynamic shimming capability. As susceptibility effects increase linearly with

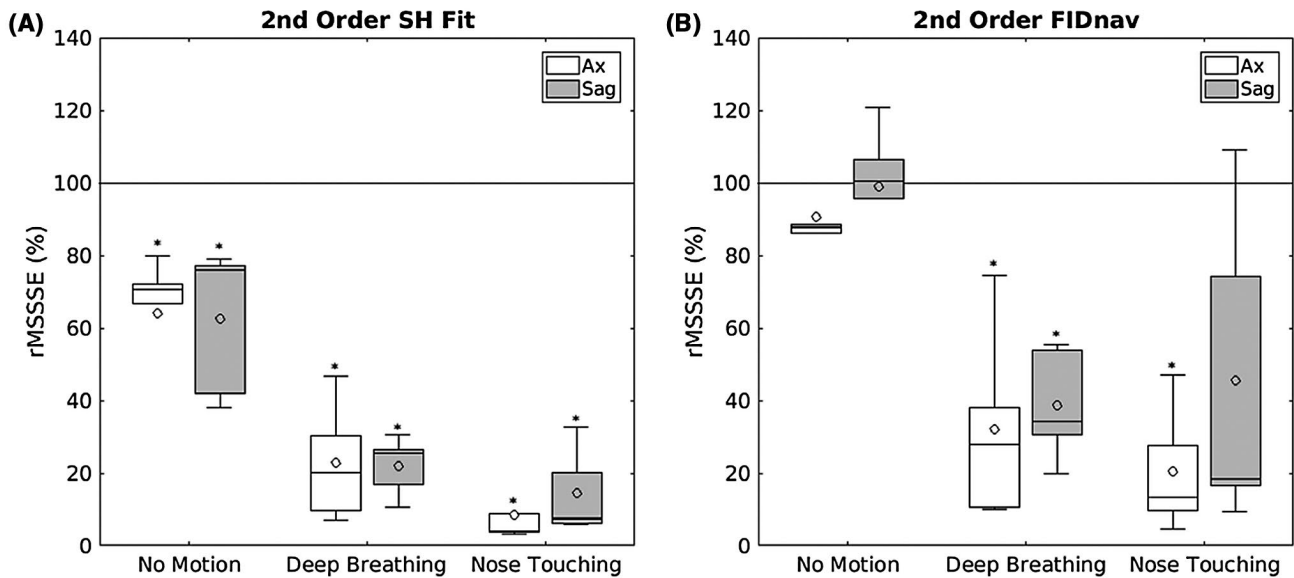


FIGURE 5 Boxplots showing the relative mean sum-of-squares error (rMSSE) in percent of the estimated field maps across all 5 volunteers for “gold standard” second-order SH fitting to the measured pixel-wise field maps (A) and from second-order inhomogeneity coefficients estimated from FIDnavs (B) in axial and sagittal planes for no motion, deep-breathing, and nose-touching tasks. Errors below 100% denote an improvement relative to no correction. FIDnav field estimates accounted for a significant ($P < 0.05$; denoted by *) proportion of the field variance induced by breathing and motion paradigms. The boxes encapsulate data between the first and third quartiles, with whiskers extending to the most extreme points not considered outliers (defined as points more than 1.5 times the interquartile distance away from the first or third quartiles, indicated as gray dots); median values are denoted by solid lines and mean values are denoted by open circles

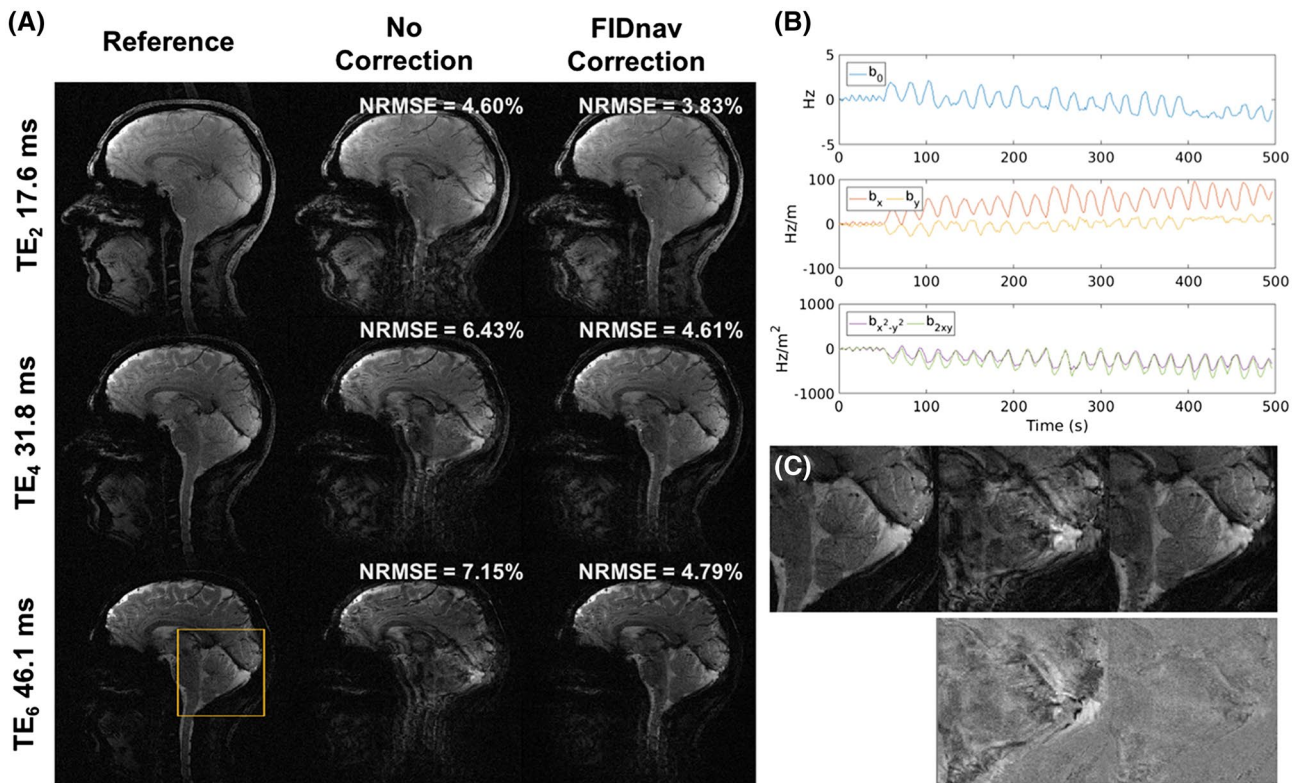


FIGURE 6 Retrospective correction results for high-resolution, sagittal 2D FLASH images acquired at different TEs in a volunteer performing the deep breathing task. Normalized root-mean-square error (NRMSE) is shown for uncorrected and FIDnav-corrected scans, relative to the reference image (A); dynamic zero-, first-, and second-order field inhomogeneity coefficients measured using FIDnavs during deep breathing (B); zoomed-in sections showing the improvement in image quality in the cerebellum following retrospective correction, and difference images (relative to the reference) before and after correction (C). Dynamic ΔB_0 measurement and correction using the proposed FIDnav method enables a dramatic improvement in T_2^* -weighted image quality

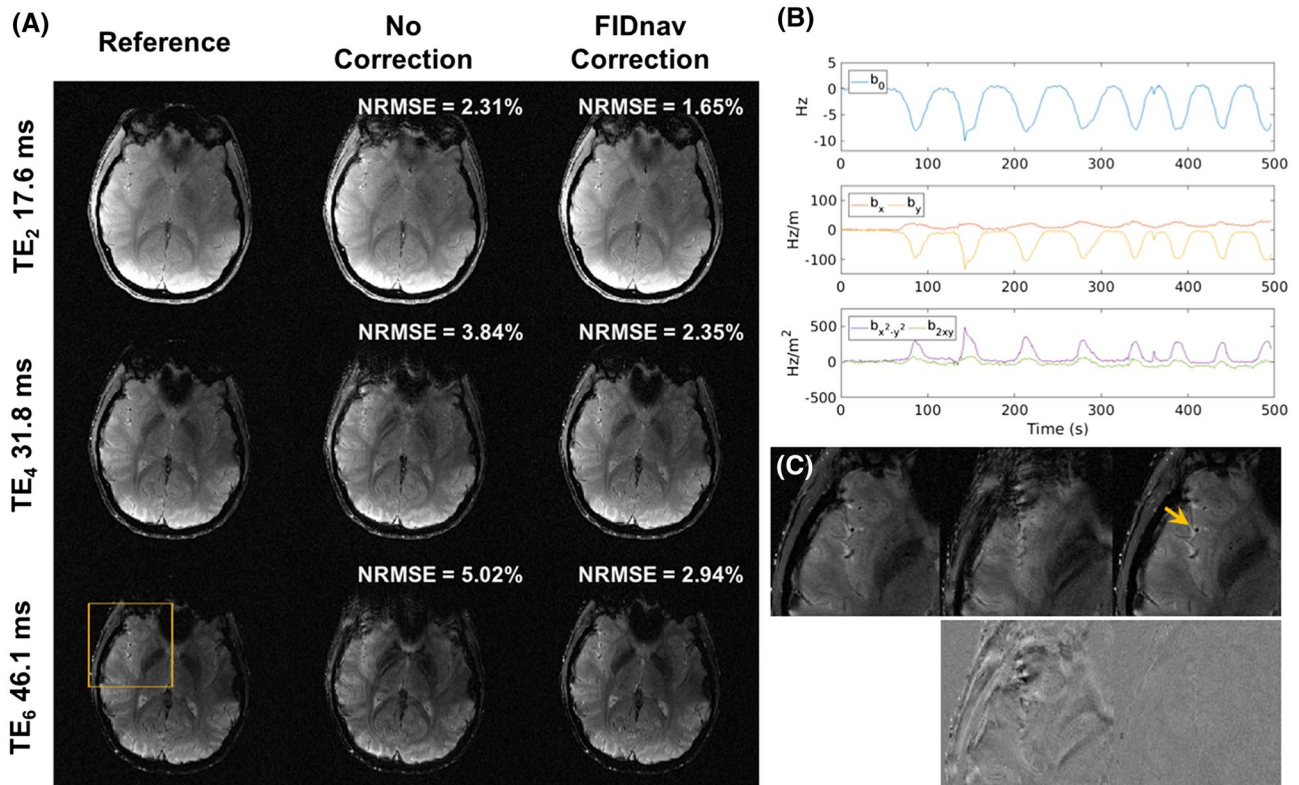


FIGURE 7 (A) Retrospective correction results for high-resolution axial 2D FLASH images acquired at different TEs in a volunteer performing the nose touching task. (B) Dynamic field inhomogeneity coefficients measured using FIDnavs during nose touching. (C) Zoomed-in sections showing improvement in image quality and difference images before and after retrospective correction in T_2^* -weighted imaging, yellow arrow highlights a clear improvement in anatomical features following FIDnav field correction

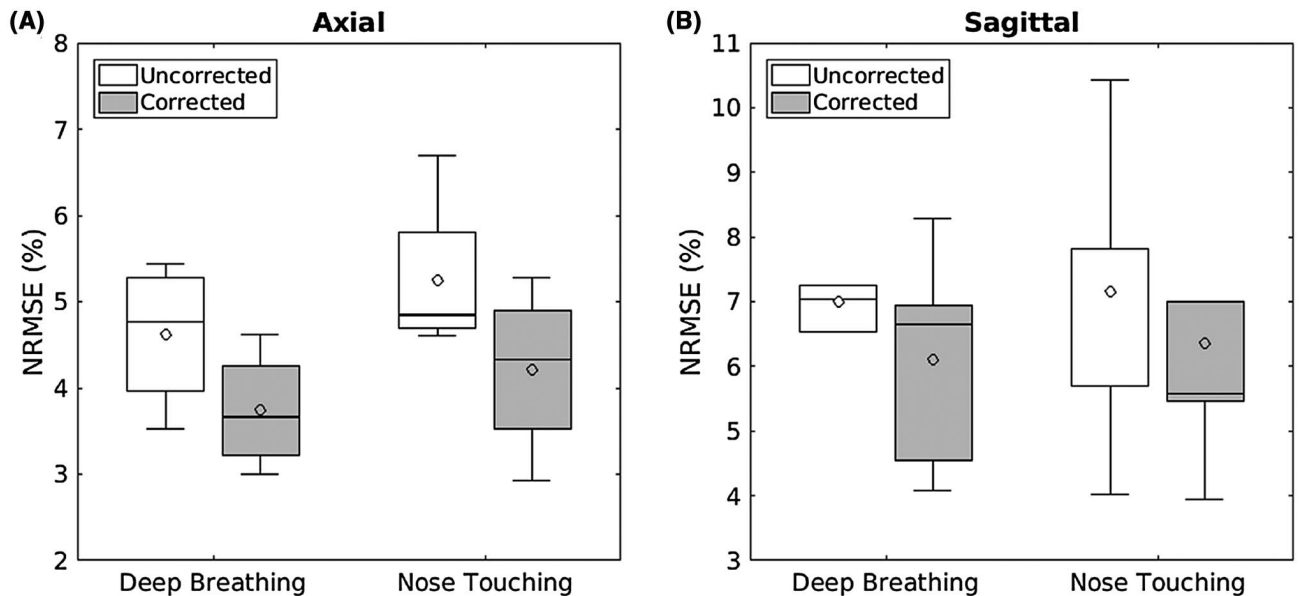
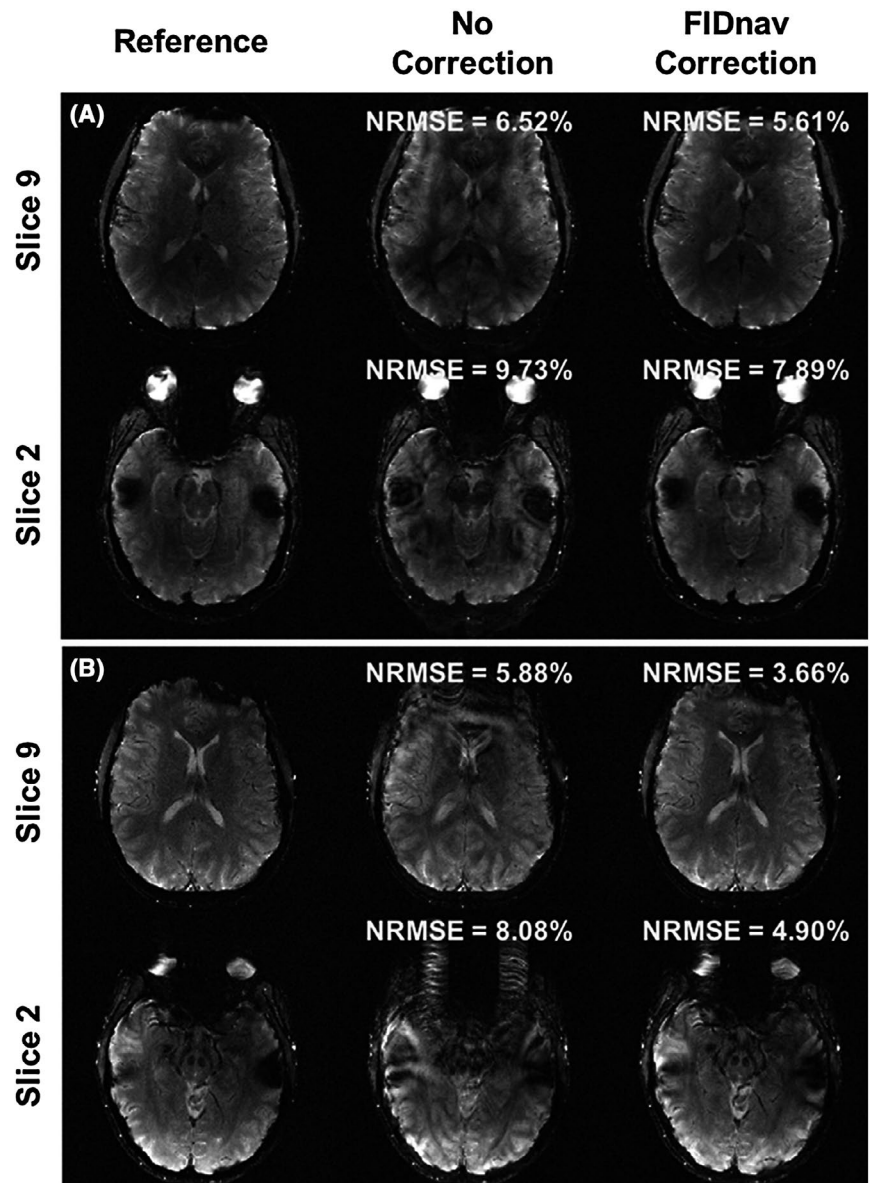


FIGURE 8 Boxplots showing normalized root-mean-square error (NRMSE) in percent across 5 volunteers, before and after retrospective correction of axial (A) and sagittal (B) T_2^* -weighted images (longest TE) acquired during deep breathing and nose touching. The boxes encapsulate data between the first and third quartiles, with whiskers extending to the most extreme points not considered outliers; median values are denoted by solid lines and mean values are denoted by open circles

FIGURE 9 Retrospective correction results for the axial multi-slice T_2^* -weighted acquisition; 2 superior and inferior slices are shown for deep breathing (A) and nose touching (B). The proposed approach successfully mitigates artifacts in multi-slice T_2^* -weighted imaging by compensating for the effects of dynamic ΔB_0 inhomogeneities in each slice



field strength, fitting for higher-order coefficients may be necessary to accurately model breathing and motion-induced field changes at 7T. As dedicated shim arrays become more readily available,⁷ the use of higher-order FIDnav correction at 7T will be explored in future work.

Our proposed framework relies on the assumption that the relative position of the spin density distribution and the coil sensitivities remains constant for the duration of the scan. This is likely to be a cause of residual errors in the field map estimation (and remaining artifacts in T_2^* -weighted images) as relative motion between the object and coil is an additional source of FIDnav signal variations.^{26,27} This may explain why FIDnav field inhomogeneity estimation for the nose-touching task in the sagittal plane was less robust in some volunteers, as movement of the hand within the excited slice represents an additional source of FIDnav signal changes that is not accounted for

in the model. Volunteers were instructed to lie as still as possible to minimize the impact of head motion on estimates of field changes and head motion was monitored using an external tracking device. FIDnav field maps were in good agreement with measured values, suggesting that small head movements <1 mm/ $^\circ$ do not substantially affect the field measurements. It is expected that the accuracy of the proposed B_0 field measurement approach would suffer in the presence of larger head movements as relative motion of the coil profiles is currently not considered in the model. Rotations of the head relative to the main magnetic field direction are also known to induce substantial magnetic field changes.⁶ Characterization of the relationship between motion and susceptibility-induced field changes is a subject of ongoing research. Future work will explore an extended model that considers the effects of both motion and field changes on the measured FIDnavs.

4.2 | Impact of retrospective correction

The deep-breathing and nose-touching tasks both resulted in substantial ghosting, blurring, and intensity modulation artifacts, which became increasingly prominent at longer TEs. Artifacts were noticeably reduced by incorporating spatiotemporal FIDnav field inhomogeneity estimates in the reconstruction, resulting in improved visualization of anatomical details. The improvement in quantitative image quality (NRMSE) across all volunteers demonstrates the ability of FIDnavs to accurately capture continuous spatially varying field changes in real-time.

In this work, we corrected for dynamic second-order SH field changes measured using FIDnavs as a proof of concept of the proposed approach. This requires an iterative reconstruction strategy, which substantially increases the reconstruction time. Reconstruction was accelerated by limiting the number of iterations and by reducing the number of channels using a coil compression approach. Restricting field correction to first-order changes would reduce the computational burden, as linear field inhomogeneities can be expressed as shifts in the underlying k-space points. The additional benefit of correcting for higher-order spatial field variations, versus reconstruction time, was beyond the scope of this work.

4.3 | Comparison to other FIDnav methods

Although initial studies demonstrated the use of navigator echoes to correct for global frequency fluctuations in fMRI,^{13,14} a variety of methods have since been proposed to encode FIDnav signals to measure spatially resolved field changes. Most approaches, including ours, require a reference scan to calibrate the spatial B_0 measurements. However, unlike other methods that require the subject to cooperate for a training session involving deep-breathing tasks,^{12,19} our approach does not require any patient interaction as the effect of field changes on FIDnav signals is calibrated entirely through a simulation step. Our proposed framework also offers several key advantages over the method used by Versluis et al.,⁵ who used multi-channel coil sensitivity information to weight the relative contribution of each (frequency-encoded) navigator echo to provide an approximation of the B_0 field: (1) it provides rapid and direct estimation of B_0 inhomogeneity coefficients without phase unwrapping or fitting to pixel-wise field maps; (2) it does not require any gradient encoding (or a priori knowledge of the direction of expected field variations); and (3) it does not require explicit calculation of a coil sensitivity map as the coil sensitivities are inherently encoded within the reference image.

Another important distinction of our proposed framework lies in how ΔB_0 is calculated. Most field measurement approaches rely on 2 or more measurements with different TEs and assume that phase changes are linear within a voxel.^{15,17,18}

Although this assumption may be valid for spatially resolved images and projections, it breaks down for unencoded point measurements, which represent the integral of the spin density contributions over the excitation volume. For inhomogeneous objects, phase differences are corrupted by voxel dephasing, T_2^* relaxation and chemical heterogeneity, and the relationship is no longer linear. These factors were cited by Splitthoff and Zaitsev,²⁰ who successfully estimated ΔB_0 from the temporal evolution of FIDnav signals in a phantom, as a barrier to successful implementation of their approach in vivo. Here, we estimate changes in ΔB_0 relative to a reference time point from FIDnavs sampled at the same time as TE of the reference image, therefore eliminating problems with chemical heterogeneity and relaxation.

4.4 | Applications and extensions

In this study, we measured dynamic, slice-wise inhomogeneity coefficients from FIDnavs to correct artifacts in T_2^* -weighted images induced by magnetic field distortions during deep breathing and arm motion. T_2^* -weighted imaging is being increasingly used at higher field strengths because of its high magnitude and phase contrast.²⁸ Real-time characterization of spatiotemporal field changes with FIDnavs would enable improvement of T_2^* -weighted imaging quality for a broad range of clinical applications including Alzheimer's disease,²⁹ Huntington's disease,³⁰ and stroke,³¹ as well as research into structural brain changes during healthy aging.³²

Our proposed method is simple to calibrate, requiring only acquisition of a low-resolution reference image, and FIDnavs can be added without affecting image contrast or increasing scan time. The time needed to acquire the reference data for each subject could be reduced using parallel imaging, imaging at a lower resolution, or by applying a pre-calculated offset to compensate for gradient delays. This approach can be easily extended to 3D imaging, by acquiring a 3D reference image, and simulating SH coefficient changes in the third dimension. This would require 4 inhomogeneity coefficients to model first-order changes and a total of 9 coefficients to model changes up to second order. Extension to other sequences is also possible (e.g., to provide distortion correction in EPI). This would require generation of a suitable reference image with matched contrast to simulate the FIDnav signal in the host sequence.³³ Inserting an FIDnav module increases the minimal TE by the duration of the navigator, which is not a problem for anatomical T_2^* -weighted imaging but may be a limitation for protocols that do not have a time delay to accommodate the FIDnav. Another minor limitation is that application to techniques involving dynamic signal changes (e.g., dynamic susceptibility contrast) will be challenging, as this represents an additional source of signal variation, not related to field changes.

5 | CONCLUSIONS

In summary, we demonstrate that spatiotemporal ΔB_0 changes up to second order can be characterized by the proposed FIDnav method. FIDnav field estimates account for a significant proportion of the field variance induced by deep breathing and arm motion and can be acquired extremely rapidly, making this approach highly suited for continuous field monitoring and real-time shimming applications. By incorporating dynamic FIDnav field inhomogeneity measurements into the image reconstruction, we demonstrate dramatic improvement in T_2^* -weighted image quality in the presence of strong B_0 field modulations.

ACKNOWLEDGMENTS

This research was supported in part by NIH grants R01 EB019483, R01 NS079788, R01 DK100404, R44 MH086984, IDRC U54 HD090255, and by an Early Career Award from the Thrasher Research Foundation.

CONFLICT OF INTEREST

Dr. Tobias Kober is an employee of Siemens Healthcare.

ORCID

Tess E. Wallace  <https://orcid.org/0000-0002-8519-5913>

Onur Afacan  <https://orcid.org/0000-0003-2112-3205>

REFERENCES

- Versluis MJ, Peeters JM, van Rooden S, et al. Origin and reduction of motion and f_0 artifacts in high resolution T_2^* magnetic resonance imaging: application in Alzheimer's disease patients. *Neuroimage*. 2010;51:1082–1088.
- Haacke EM, Xu Y, Cheng YN, Reichenbach R. Susceptibility weighted imaging (SWI). *Magn Reson Med*. 2004;52:612–618.
- van de Moortele PF, Pfeuffer J, Glover GH, Ugurbil K, Hu X. Respiration-induced B_0 fluctuations and their spatial distribution in the human brain at 7 Tesla. *Magn Reson Med*. 2002;47:888–895.
- Verma T, Cohen-Adad J. Effect of respiration on the B_0 field in the human spinal cord at 3T. *Magn Reson Med*. 2014;72:1629–1636.
- Versluis MJ, Sutton BP, De Bruin PW, Bornert P, Webb A, van Osch MJ. Retrospective image correction in the presence of nonlinear temporal magnetic field changes using multichannel navigator echoes. *Magn Reson Med*. 2012;68:1836–1845.
- Liu J, de Zwart JA, van Gelderen P, Murphy-Boesch J, Duyn JH. Effect of head motion on MRI B_0 field distribution. *Magn Reson Med*. 2018;80:2538–2548.
- Stockmann JP, Wald LL. In vivo B_0 field shimming methods for MRI at 7 T. *Neuroimage*. 2018;168:71–87.
- Duerst Y, Wilm BJ, Wyss M, et al. Utility of real-time field control in T_2^* -weighted head MRI at 7T. *Magn Reson Med*. 2016;76:430–439.
- Wilm BJ, Barmet C, Pavan M, Pruessmann KP. Higher order reconstruction for MRI in the presence of spatiotemporal field perturbations. *Magn Reson Med*. 2011;65:1690–1701.
- Kasper L, Bollmann S, Vannesjo SJ, et al. Monitoring, analysis, and correction of magnetic field fluctuations in echo planar imaging time series. *Magn Reson Med*. 2015;74:396–409.
- Vannesjo SJ, Miller KL, Clare S, Tracey I. Spatiotemporal characterization of breathing-induced B_0 field fluctuations in the cervical spinal cord at 7T. *Neuroimage*. 2018;167:191–202.
- Wezel J, Boer VO, van der Velden TA, et al. A comparison of navigators, snap-shot field monitoring, and probe-based field model training for correcting B_0 -induced artifacts in T_2^* -weighted images at 7 T. *Magn Reson Med*. 2017;78:1373–1382.
- Hu X, Kim SG. Reduction of signal fluctuation in functional MRI using navigator echoes. *Magn Reson Med*. 1994;31:495–503.
- Pfeuffer J, van de Moortele PF, Ugurbil K, Hu X, Glover GH. Correction of physiologically induced global off-resonance effects in dynamic echo-planar and spiral functional imaging. *Magn Reson Med*. 2002;47:344–353.
- Ward HA, Riederer SJ, Jack CR. Real-time autoshimming for echo planar timecourse imaging. *Magn Reson Med*. 2002;48:771–780.
- van der Kouwe AJW, Benner T, Dale AM. Real-time rigid body motion correction and shimming using cloverleaf navigators. *Magn Reson Med*. 2006;56:1019–1032.
- Alhamud A, Taylor PA, van der Kouwe AJW, Meintjes EM. Real-time measurement and correction of both B_0 changes and subject motion in diffusion tensor imaging using a double volumetric navigated (DvNav) sequence. *Neuroimage*. 2016;126:60–71.
- Gretsch F, Marques JP, Gallichan D. Investigating the accuracy of FatNav-derived estimates of temporal B_0 changes and their application to retrospective correction of high-resolution 3D GRE of the human brain at 7T. *Magn Reson Med*. 2018;80:585–597.
- van Gelderen P, de Zwart JA, Starewicz P, Hinks RS, Duyn JH. Real-time shimming to compensate for respiration-induced B_0 fluctuations. *Magn Reson Med*. 2007;57:362–368.
- Splitthoff DN, Zaitsev M. SENSE shimming (SSH): a fast approach for determining B_0 field inhomogeneities using sensitivity coding. *Magn Reson Med*. 2009;62:1319–1325.
- Powell MJD. *The BOBYQA algorithm for bound constrained optimization without derivatives*. Cambridge; 2009. http://www.damtp.cam.ac.uk/user/na/NA_papers/NA2009_06.pdf. Accessed May 1, 2017.
- Afacan O, Erem B, Roby DP, et al. Evaluation of motion and its effect on brain magnetic resonance image quality in children. *Pediatr Radiol*. 2016;46:1728–1735.
- Zhang T, Pauly JM, Vasanaawala SS, Lustig M. Coil compression for accelerated imaging with Cartesian sampling. *Magn Reson Med*. 2013;69:571–582.
- Walsh DO, Gmitro AF, Marcellin MW. Adaptive reconstruction of phased array MR imagery. *Magn Reson Med*. 2000;43:682–690.
- Sengupta S, Welch EB, Zhao Y, et al. Dynamic B_0 shimming at 7 Tesla. *Magn Reson Imaging*. 2011;29:483–496.
- Kober T, Marques JP, Gruetter R, Krueger G. Head motion detection using FID navigators. *Magn Reson Med*. 2011;66:135–143.
- Wallace TE, Afacan O, Waszak M, Kober T, Warfield SK. Head motion measurement and correction using FID navigators. *Magn Reson Med*. 2019;81:258–274.
- Duyn JH, van Gelderen P, Li T, de Zwart JA, Koretsky AP, Fukunaga M. High-field MRI of brain cortical substructure based on signal phase. *Proc Natl Acad Sci U S A*. 2007;104:11798–11801.

29. van Rooden S, Versluis MJ, Liem MK, et al. Cortical phase changes in Alzheimer's disease at 7T MRI: a novel imaging marker. *Alzheimers Dement*. 2014;10:19–26.
30. Doan NT, van den Bogaard SJA, Dumas EM, et al. Texture analysis of ultrahigh field T2*-weighted MR images of the brain: application to Huntington's disease. *J Magn Reson Imaging*. 2014;39:633–640.
31. Novak V, Abduljalil AM, Novak P, Robitaille PM. High-resolution ultrahigh-field MRI of stroke. *Magn Reson Imaging*. 2005;23:539–548.
32. Buijs M, Trung N, van Rooden S, Versluis MJ. In vivo assessment of iron content of the cerebral cortex in healthy aging using 7-Tesla T2*-weighted phase imaging. *Neurobiol Aging*. 2017;53:20–26.
33. Dragonu I, Splitthoff DN, Baxan N, Freitag P, Hennig J, Zaitsev M. Shim navigators for accurate detection of the B0 magnetic field inhomogeneities using reference MGE images. In Proceedings of the 19th Annual Meeting of ISMRM, Montreal, Canada, 2011. p. 2690.

SUPPORTING INFORMATION

Additional supporting information may be found online in the Supporting Information section at the end of the article.

FIGURE S1 Comparison between first- and second-order shim changes in a phantom, estimated by solving the inverse of Equation 5 via least-squares fitting (linear approximation) (A); and using a non-linear optimization algorithm to solve Equation 4 (direct fitting) (B). Solid line denotes the applied shim currents; filled circles with error bars show the mean and SD of FIDnav measurements in each scan; gray crosses denote results of direct SH fitting to pixel-wise field maps. Both methods yield highly similar results, validating the use of a linear approximation for the range of field changes tested in this study

FIGURE S2 Comparison of zeroth-, first-, and second-order inhomogeneity coefficients measured from SH fitting and FIDnavs across all volunteers performing the deep-breathing

task (sagittal plane; A) and across all volunteers performing the nose-touching task (axial plane; B)

FIGURE S3 Dynamic field inhomogeneity coefficient estimates corresponding to the more superior (slice 9) and inferior (slice 2) brain regions shown in Figure 9 for the deep-breathing (A) and nose-touching (B) experiments

FIGURE S4 Comparison of adaptive combine reconstruction results for 64-channel head coil (A) and compression with 16 virtual channels (B). Coil compression accelerates reconstruction while maintaining highly similar image quality (C)

FIGURE S5 Boxplots showing the relative mean sum-of-squares error (rMSSE) in percent of the estimated field maps across all 5 volunteers for spherical harmonic (SH) coefficients up to third order estimated by direct SH fitting to pixel-wise field maps and estimated from the measured FIDnavs in axial (A) and sagittal (B) planes. Errors below 100% denote an improvement relative to no correction. No substantial differences were found between field maps generated from first-, second-, or third-order SH coefficients estimated from FIDnavs for the field changes observed in this study

TABLE S1 Accuracy (mean absolute error) and precision (SD of error) of zeroth-, first-, and second-order FIDnav inhomogeneity coefficients, compared to the results of direct SH fitting to measured field maps in axial and sagittal planes across 5 volunteers performing deep-breathing and nose-touching tasks. Maximum field changes for each paradigm are shown in brackets

How to cite this article: Wallace TE, Afacan O, Kober T, Warfield SK. Rapid measurement and correction of spatiotemporal B₀ field changes using FID navigators and a multi-channel reference image. *Magn Reson Med*. 2019;00:1–15. <https://doi.org/10.1002/mrm.27957>